SCIENTIFIC REPORTS

OPEN

Tunable Magneto-Optical Kerr Effects of Nanoporous Thin Films

Weiwei Zhang[1], Jianjun Li[1], Xiaokun Ding[2], Philippe Pernod[2], Nicolas Tiercelin[2] & Yujun Song[1]

Magnetoplasmonics, combining magnetic and plasmonic functions, has attracted increasing attention owing to its unique magnetic and optical properties in various nano-architectures. In this work, Ag, CoFeB and ITO layers are fabricated on anodic aluminum oxide (AAO) porous films to form hybrid multi-layered nanoporous thin films by magnetron sputtering deposition process. The designed nanostructure supports localized surface plasmon resonance (LSPR) and tunable magneto-optical (MO) activity, namely, the sign inversion, which can be controlled by AAO porous film geometry (pore diameter and inter-pore spacing) flexibly. The physical mechanism of this special MO phenomena is further analyzed and discussed by the correlation of Kerr rotation and electronic oscillations controlled by the surface plasmon resonance that is related to the nanoporous structure.

Plasmonics[1, 2] preserves varieties of applications in high dimentional data storage[3–8], high sensitive chemical detection[9–13], biosensing[14–19] and so forth[20]. This is mainly attributed to the ability of surface plasmons to conduct the subdiffraction-limit of light, to enhance the local surface electromagnetic fields[21] or to allow localization of light at nanoscale dimensions[22]. It has been reported that plasmonic properties of metal nanoparticles intrinsically rely on their size, shape, surface topography, crystal structure, inter-particle spacing and dielectric environment[23, 24]. One development in plasmonics is magnetoplasmonics. Magnetoplasmonics promotes great interests on the momentum in photonics and magnetism sectors that are concerned with the resonant enhancement of light-magnetic-matter interaction[25] with the rapid development of nanofabrication techniques[26] (e.g., nanoimprint[27, 28], lithography[29–35], physical vapor deposition[36, 37] and microfluidic synthesis process[38–40]). One topic in magnetoplasmonics is the enhancement of the magneto-optical effects in plasmonic nanostructures[41]. Magnetoplasmonics in nanostructures has potential to provide the flexibility in the reception and emission of photon and the light control at nanoscale, which are crucial in lots of emergent nano-optical applications[42]. For instance, when an incident light beam is well coupled to surface plasmon polartions inside the noble metal film (e.g., Ag[43–45] and Au[46–48]) that has been deposited on magnetic components (e.g., Co, CoFeB, CoPt and NiO) and then reflected back to the optical field, its properties (e.g., intensity and the polarization status) become much sensitive to the medium permittivity and magnetization[49].

The polarization status of light, used as information carriers, not only has great potential in biochemosensing[50], optical communications and ultra-sensitive imaging[51], but also plays important roles in the photonic transfer of quantum information[52, 53]. A coupled model of incoming electromagnetic excitation and the collective oscillation of free-electrons near the surface of metallic nanostructures has attracted more and more attention owing to their enhanced plamonic and magneto-optical properties[54], such as enhanced Raman scattering[55, 56], tunable nonlinear optical effects, surface plasmon polariton (SPP) and magneto-optical (MO) effects (i.e., Zeeman, Faraday or Kerr effects)[37, 57–62].

Anomalous magneto-optical Kerr effects (MOKE) phenomena have been observed in various nanostructures[36, 50, 63, 64]. Localized surface plasmon resonance (LSPR) can be exploited in controlled manipulation of the MO response of nanostructured ferromagnetic nickel nanodisks, in which the inversed Kerr rotation is observed[50]. Calculations of bi-layered perforated nanostructure films formed by a gold layer and a smooth iron garnet layer show much higher transverse MOKE than the bare garnet film[57]. Hexagonally arrayed ferromagnetic nanowire films exhibit an enhanced Kerr rotation, which shows a strong dependence on nanowire diameters[65]. Optical and MO properties of hexagonally arrayed ferromagnetic nanoporous films show a complex MO spectrum with a much higher polarization rotation than that of the pure Co film[66, 67]. And some other systems accompanied by the enhanced MO response like Au/Co/Au nanosandwiches[68, 69], gold-coated maghemite nanoparticles[70], ferromagnetic garnet films incorporating Au nanoparticles[71], Co@Ag core-shell nanoparticles[72] and

[1]Department of Applied Physics, Center for Modern Physics Technology, Beijing Key Laboratory for Magneto-Photoelectrical Composite and Interface Science, University of Science and Technology Beijing, Beijing, 100083, China. [2]Univ. Lille, CNRS, Centrale Lille, ISEN, Univ. Valenciennes, UMR 8520-IEMN-LIA LICS, F-59000, Lille, France. Correspondence and requests for materials should be addressed to Y.S. (email: songyj@ustb.edu.cn)

Co/Pt multi-layers deposited on polystyrene sphere arrays[73] are also reported to have unique localized and/or propagating resonant excitations[50]. However, little attention has been paid on the nanoporous films consisting of noble metals, dielectrics and magnetic materials, which support strong LSPR and special MO response.

Anodic aluminum oxide (AAO) porous film, long-range ordered self-organized[74] hexagonal columnar cells with central, cylindrical, uniform size holes, can be fabricated by the traditional 2-step anodizing process[23, 75, 76] economically. This special nanoporous structure is assigned to the mechanical stress at the aluminum/alumina interface. This is proposed to cause repulsive forces between the neighboring pores[75]. The porous film is a useful template in the fabrication of devices[76] (e.g., photoelectronic device[77] and nanoparticle assemblies[78] whose interfacial interaction can be regulated by the AAO structure, such as pore size, membrane thickness and surface morphologies) and various functional nanostructures[79–82] (e.g., solar cells[83], nanotubes[84–86], nanofibers[86], catalysts[87–89], and metal nanowires[90]). To date, the AAO porous film also has a wide applications in ultrafiltration[91], biosensors[92–94], photonics[95, 96], masking[97] and information storage[98]. Many types of nanocomposites have been fabricated on the AAO porous film by magnetron sputtering deposition process and the deposited thin films can form a densely packed, regular and almost petal like structure around the pores[99]. This special structure permits an opportunity to realize LSPR, to enhance Fabry-Pérot interferences[11] and to tailor magneto-optical Kerr effects.

In this work, a porous nanostructure with intertwined plasmonic and magnetic properties is developed via depositing Ag, CoFeB and ITO layers on morphology controlled AAO porous film to form hybrid multi-layered nanoporous films by a magnetron sputtering deposition process. From the analysis of the experimental data, the nanoporous structure supports localized surface plasmon resonance and tunable inversion of MOKE hysteresis loops.

Results

Morphology and Composition.
To study the effect of the AAO porous film geometry on the surface plasmon activity and MOKE inversion, the inter-pore spacing of two AAO substrates was first set to two different values (i.e., 110 nm and 450 nm). Then, the pore diameter of three samples with the same inter-pore spacing 110 nm was set to 40 nm, 60 nm and 100 nm. Similarly, the pore diameter of three samples with the same inter-pore spacing 450 nm was set to 130 nm, 160 nm and 200 nm. Finally, hybrid multi-layered films Ag (5 nm)/ITO (10 nm)/CoFeB (10 nm)/ITO (10 nm)/Ag (5 nm) were fabricated on the prepared AAO templates. Thus, six hybrid multi-layered samples with different nanoporous geometries were fabricated and characterized.

Fig. 1 gives the typical top view SEM images of the already fabricated hybrid multi-layered nanoporous films. After deposition, the surface morphologies of the samples become more distinct and comparable with the changes of the AAO pore diameter (D) and inter-spacing (S). From the local-magnified angle-tilted SEM image (schemed in the Fig. 2a) of sample (b) (S = 110 nm, D = 60 nm), it is clearly noticed that most holes approximately present a nanofunnel morphology (the red circle is larger than the green one). A simplified nanostructure is sketched in Fig. 2b. EDS (Fig. 2c) confirms the existence of Ag, Co, Fe, In, Sn and O elements in the films and they originate from the deposited Ag layer, CoFeB layer and ITO layer[36, 100] respectively.

Magneto-Optical Kerr Rotation and Magnetic Domain.
Fig. 3a shows the polar magneto-optical Kerr effect (P-MOKE) hysteresis loops of the prepared six nanoporous samples. At the first glance, it is evidently verified that an anomalous inversed Kerr hysteresis is observed by modifying the AAO porous film geometries (pore diameter and inter-spacing). Similarly, the sign inversion is also detected in the longitudinal magneto-optical Kerr effect (L-MOKE) configuration simultaneously (Fig. 3b). It has been clarified that the sign of the MOKE is defined by both incoming and reflecting polarization of light, and a clockwise or an anticlockwise axis determines the sign change[50]. However, when the same incoming polarization and the same axis of the polarization ellipse viewed along the reflected direction are used, the inversion information in both P-MOKE and L-MOKE can be definitely observed.

The dramatic changes of the sign inversion can also be reflected by the direction rotation of typical magnetic domains (represented by the color mapping rotation, Fig. S1 in Supplementary Information) with the external applied magnetic field along the longitudinal direction of the samples. The first two samples ((I) S = 110 nm, D = 40 nm and (II) S = 110 nm, D = 60 nm) display an apparent color change rotation with the magnetic field changing from 1200 Oe (a), to 600 Oe (b), 0 Oe (c), −600 Oe (d), −1200 Oe (e), and back to -600 Oe (f), 0 Oe (g), 600 Oe (h) and 1200 Oe (i). However, as both the AAO pore diameters and inter-pore spacing are further increased (S = 450, D = 130 nm and S = 450 nm, D = 160 nm), directions of the magnetic domain distribution (as relatively indexed by the field intensity, or color change) distinctly show opposite behavior. Another result worth noting is that the magnetic domain distribution is not so distinctively exhibited when the AAO pore diameters are 100 nm (Fig. S1(III)) and 200 nm (Fig. S1(VI)), possibly due to the much reduced wall thickness among pores.

Therefore, under certain conditions, the sign of the MOKE loops in our proposal system is related to the pore diameter and inter-spacing. Thus, changing the AAO pore geometry allows us to tailor the MOKE sign. In order to unambiguously illustrate the physical mechanism of nanoporous structure related MO phenomena, the surface plasmon resonance property was investigated.

Optical response.
Fig. S2 in the Supplementary Information gives the absorbance of the pure AAO porous film (S = 110 nm, D = 60 nm) and the various films deposited on the same template. In this figure, the origin of oscillations observed in each spectrum is related to the optical modes of the Fabry-Pérot cavity[101, 102]. Furthermore, it is observed that when the Ag layer is coated on the surface of the AAO porous film, the absorbance intensity and amplitude of Fabry-Pérot interference resonances are greatly enhanced. It is well known that the noble metal Ag with a very high electrical conductivity can provide abundant free electrons, which can well couple with the electromagnetic (EM) field of light to generate the surface plasmon resonance. For the special designed hybrid multi-layered nanoporous structure (Ag (5 nm)/ITO (10 nm)/CoFeB (10 nm)/ITO (10 nm)/Ag
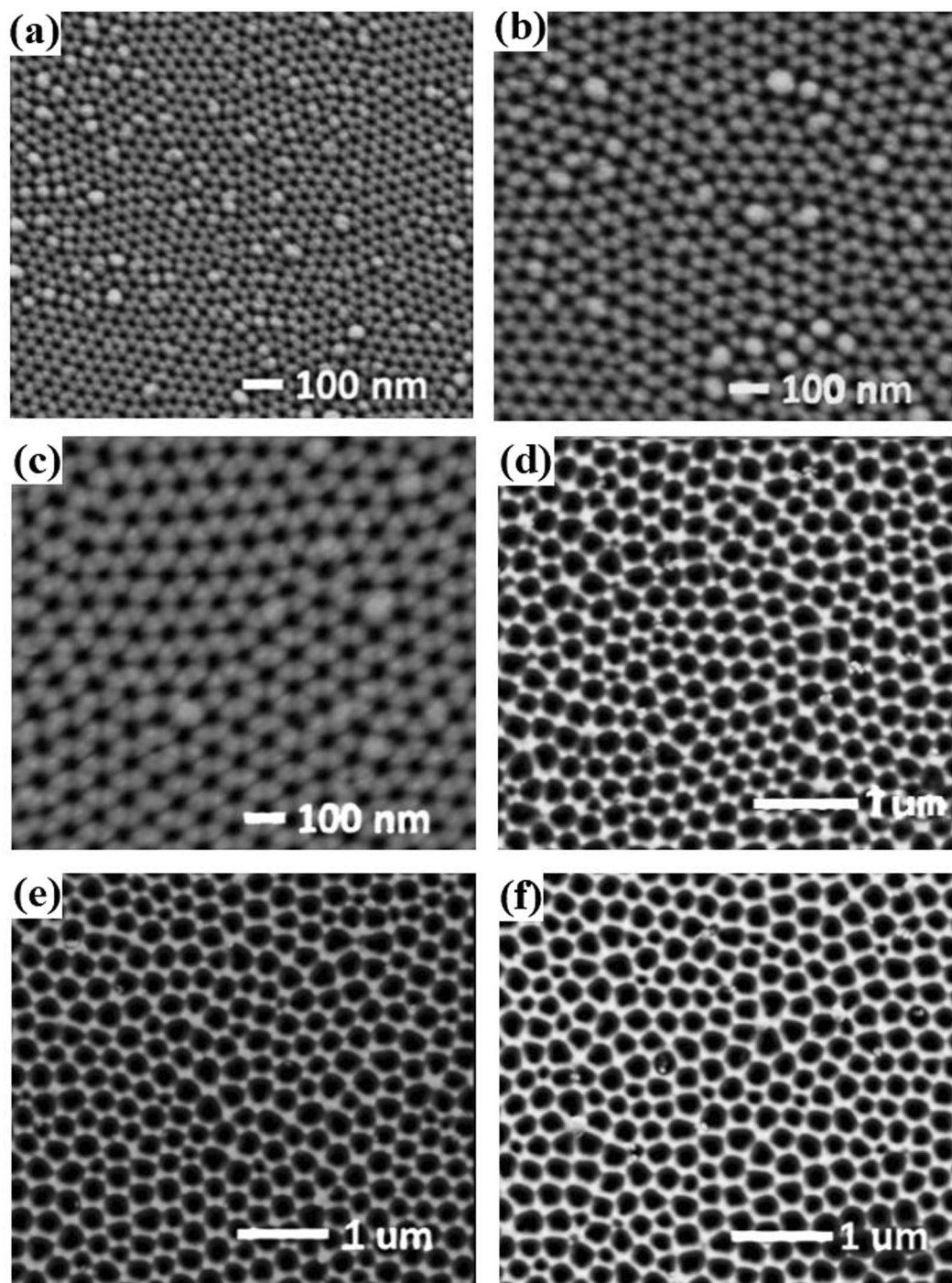
Figure 1. Top-viewed SEM images of multi-layered nanoporous arrayed films deposited on six AAO templates with different geometries (**a**) S = 110 nm, D = 40 nm, (**b**) S = 110 nm, D = 60 nm, (**c**) S = 110 nm, D = 100 nm, (**d**) S = 450 nm, D = 130 nm, (**e**) S = 450 nm, D = 160 nm and (**f**) S = 450 nm, D = 200 nm.

(5 nm)) with a highly specific surface area, the resonance can be excited not only on the surface of the nanopore film but also localized around the pore side and the inner part of the pore.

Fig. 4a shows the optical absorbance of the prepared samples, whose resonances present an apparent Fabry-Pérot interference usually existing in the nanohole films[37]. Clearly, for the same inter-pore spacing 110 nm, the peaks exhibit a blue shift with the nanopore diameter increase from 40 nm, to 60 nm and to 100 nm at one optical oscillation period located between 640 nm and 900 nm (Fig. 4b). The wavelength of the laser light (660 nm) in our experiments is just in this wavelength range. Analysis of the Kerr hysteresis loops and the peak positions of the far-field absorbance intensity (Fig. 4b) indicates that there are the same signs when the peaks are at the same side of the given excitation line, while the signs are definitely inversed for those on the opposite sides (i.e., those with inter-spacing of 450 nm and diameter of 130 nm, 160 nm and 200 nm). From previous studies of
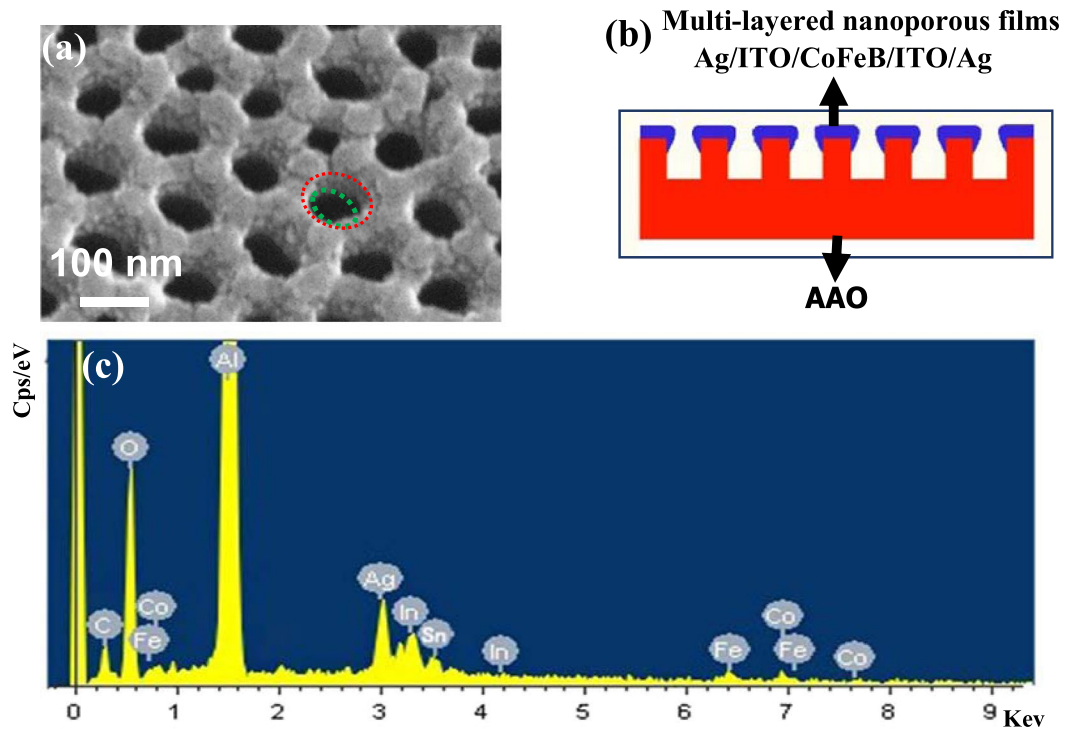
Figure 2. (**a**) Angle tilted magnified SEM images of Ag (5 nm)/ITO (10 nm)/CoFeB (10 nm)/ITO (10 nm)/Ag (5 nm) nanoporous films on S = 110 nm, D = 60 nm AAO template, (**b**) scheme of the cross-section of nanofunnel films and (**c**) EDS of one of multi-layered nanoporous films suggesting that these films have Ag, Co, Fe, Sn, In, Al and O elements.

magnetoplasmonics, oscillation shapes of the absorbance efficiency are directly related to the surface plasmon resonance[103–105]. Thus, it is concluded that the special MO phenomena are well related to the surface plasmon resonance which can be controlled by the designed nanoporous system.

Discussion

The physical mechanism of the anomalous MOKE phenomena in the multi-layered nanoporous films can be unambiguously clarified. It is well known that the coupling of the transverse magnetic model (TM or p-polarization) and the transverse electric model (TE or s-polarization) can account for the sign inversion of the MOKE rotation[106, 107]. Taking P-MOKE as an example, when the TE electron oscillation mode in the noble metal Ag surface is excited owing to the introduced s-polarization light, due to the applied magnetic field, TM electron oscillation mode can be induced as a consequence of the spin-orbit (SO) coupling. The new hybrid oscillation mode has a strong effect on the Kerr information (i.e., Kerr rotation and ellipticity) and the phases between the two modes account for the sign of the Kerr rotation. It is well known that the tunable electron oscillations can be realized by the surface plasmon resonances, which are related to the designed nanostructure. Therefore, in this work, proper choosing the AAO porous film can control the surface plasmon resonance which has an effect on the electron oscillation modes. Furthermore, tunable sign inversion can be realized.

Besides the simplified physical mechanism of our result, we provide a clear expression of AAO geometry controlled effects on the MO response.

It is well known that when the magnetic field is applied to the surface of the sample, the permittivity tensor that contains nine complex components[51] can be written in the following form:

$$\varepsilon = \begin{pmatrix} \varepsilon_{xx} & i\varepsilon_1 & i\varepsilon_2 \\ -i\varepsilon_1 & \varepsilon_{yy} & i\varepsilon_3 \\ -i\varepsilon_2 & -i\varepsilon_3 & \varepsilon_{zz} \end{pmatrix} \tag{1}$$

where the diagonal component ε_{ii} ($i = x, y, z$) is the dielectric function of the non-magnetized material. This component does not depend on magnetization **M** when the first order magnetization is considered, and it has an effect only on the pure optical property. On the basis of the modified Drude model for the noble metal silver in our experiment, it can be expressed as

$$\varepsilon_{ii} \approx \varepsilon_\infty - \frac{\omega_p^2}{\omega^2 + i\gamma\omega}(i = x, y, z) \tag{2}$$
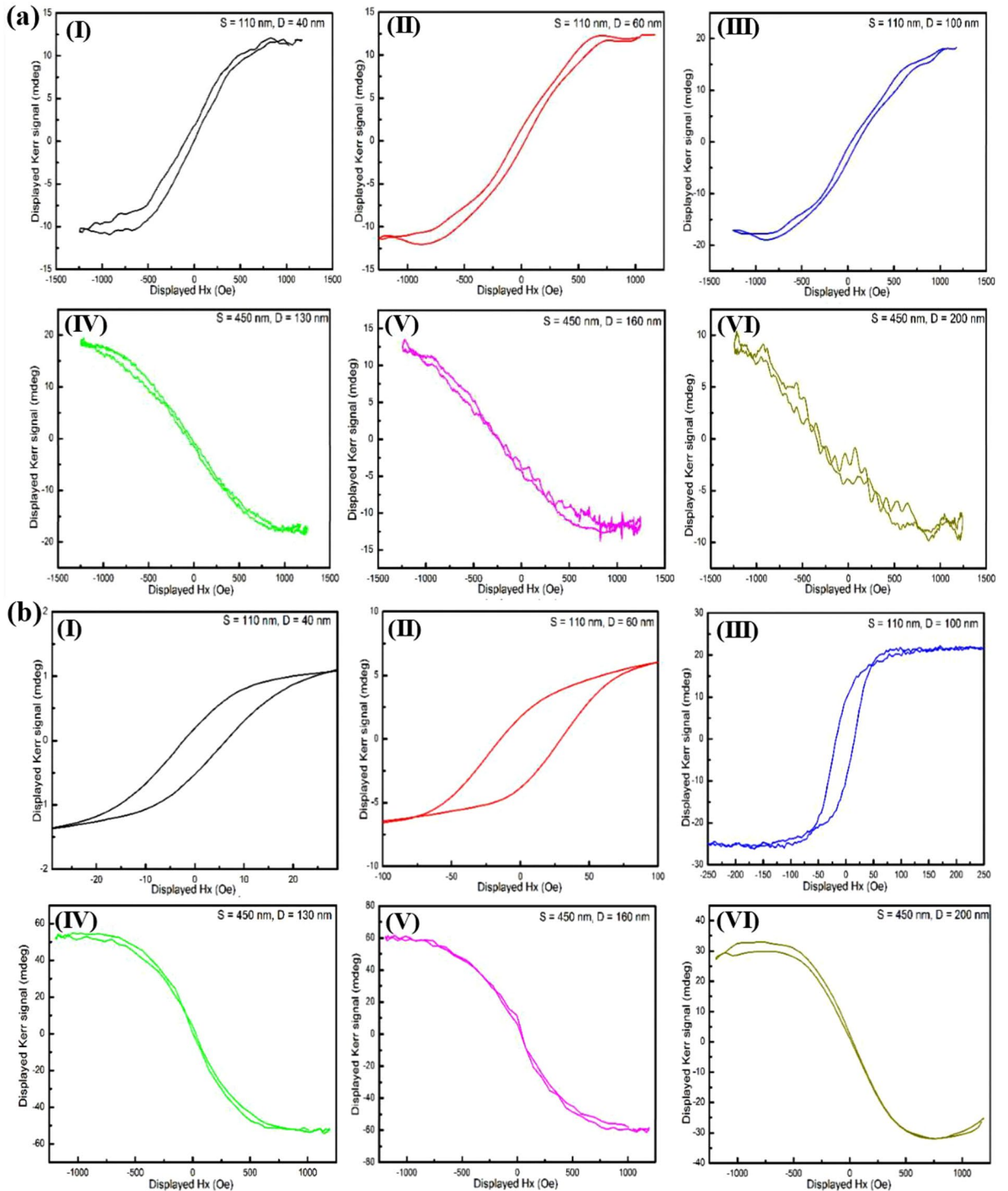
Figure 3. (**a**) P-MOKE and (**b**) L-MOKE loops of hybrid multi-layered nanoporous arrayed films deposited on six AAO templates with different geometries. (I) S = 110 nm, D = 40 nm; (II) S = 110 nm, D = 60 nm; (III) S = 110 nm, D = 100 nm; (IV) S = 450 nm, D = 130 nm; (V) S = 450 nm, D = 160 nm and (VI) S = 450 nm, D = 200 nm.

Here, ω_p is the Drude plasma frequency and $\gamma = \frac{1}{\tau}$ is the inverse electron relaxation time. The off-diagonal component ε_i ($i = 1, 2, 3$) is linearly dependent of magnetization[51]. For the different MOKE configurations, the control of the magneto-optical Kerr effect rotation originates from only one of the excited off-diagonal components ε_1, ε_2 and ε_3 when the external magnetic field is applied along the *x*, *y* or *z* direction, which are related to the P-MOKE, transversal Kerr effect (T-MOKE) or L-MOKE, respectively.
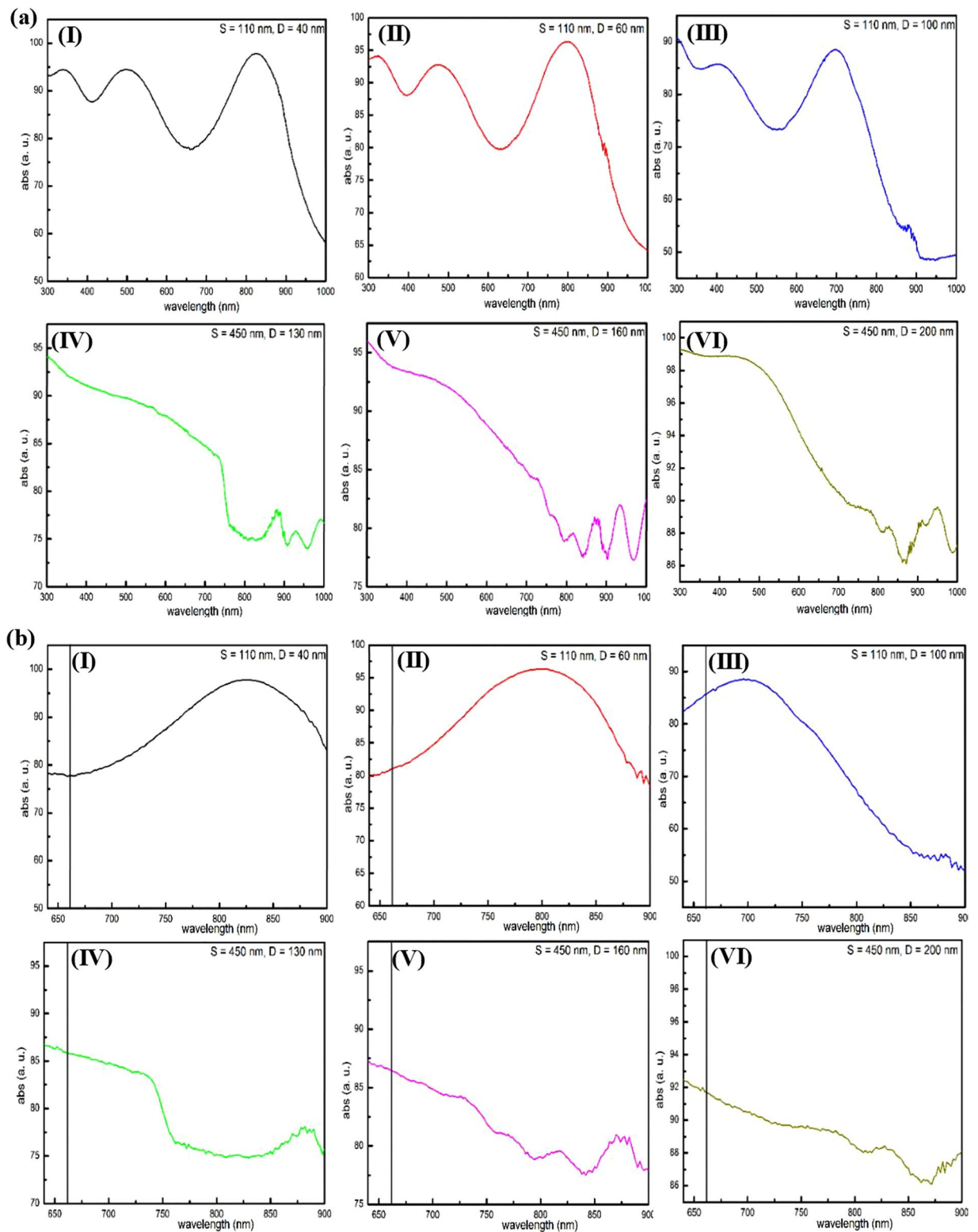
Figure 4. Absorbance intensity of hybrid multi-layered nanoporous arrayed films deposited on six AAO templates with different geometries. (I) S = 110 nm, D = 40 nm; (II) S = 110 nm, D = 60 nm; (III) S = 110 nm, D = 100 nm; (IV) S = 450 nm, D = 130 nm; (V) S = 450 nm, D = 160 nm and (VI) S = 450 nm, D = 200 nm. (**a**) Full range spectra. (**b**) Magnified local spectra with the vertical black line marks excitation at 660 nm.

For the P-MOKE in s-configurations (Fig. 5a), the off-diagonal term ε_1 is activated by the magnetization samples along the z axis, and the new permittivity tensor can be described by the equation 3 in which all the other terms are equal to zero.
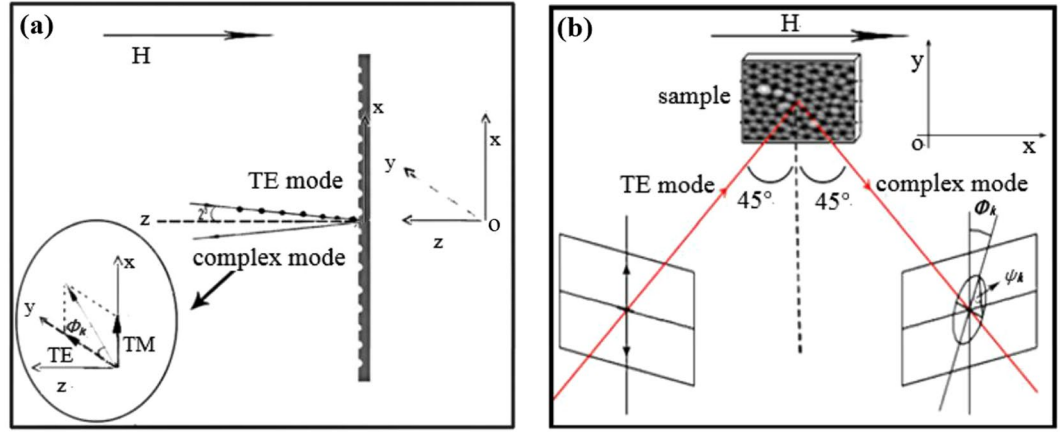
Figure 5. (**a**) P-MOKE and (**b**) L-MOKE measurement configurations.

$$\varepsilon_p = \begin{pmatrix} \varepsilon_{xx} & i\varepsilon_1 & 0 \\ -i\varepsilon_1 & \varepsilon_{yy} & 0 \\ 0 & 0 & \varepsilon_{zz} \end{pmatrix}$$

(3)

When the TE electron oscillation mode with the amplitude E_{yy} is induced as a consequence of the incident light in the wavelength of 660 nm, the light induced complex dipole along the y axis can be written as a function of the polarization α_{yy}, namely, $P_y = \alpha_{yy} E_{yy}$ (see refs [50], [51], [106], [108].). The complex dipole can be generated by the SO coupling that transfers the oscillations to the orthogonal direction.

$$P_x = \alpha_{xx} E_{so} = \alpha_{xy} E_{yy} = \frac{-i\varepsilon_1 \alpha_{xx} \alpha_{yy}}{(\varepsilon - \varepsilon_m)^2} = \alpha_{so} \alpha_{xx} \alpha_{yy} E_{yy}$$

(4)

In this expression, the constant ε_m is the dielectric function of the surrounding medium. The tuning of the phase and amplitude of the polarization can be achieved by the two orthogonal dipoles in the plane of the samples referring to our detecting system. The similar expression of the Kerr rotation in refs [1], [35] and [37] for nanoparticle arrays is used.

$$\theta_k = \text{Re}\left(\frac{P_x}{P_y}\right) + \text{Im}\left(\frac{P_x}{P_y}\right)i$$

(5)

In our investigation, we only focus on the Kerr rotation angle, named as ϕ_k.

$$
\begin{aligned}
\phi_k^p &= \text{Re}\left(\frac{P_x}{P_y}\right) = \text{Re}\left(\frac{\alpha_{so} \alpha_{xx} \alpha_{yy} E_{yy}}{\alpha_{yy} E_{yy}}\right) \\
&= \text{Re}(\alpha_{so} \alpha_{xx}) \\
&= \text{Re}(\alpha_{so}^0 e^{i\phi(\alpha_{so})} \alpha_{xx}^0 e^{i\phi(\alpha_{xx})}) \\
&= \text{Re}(\alpha_{so}^0 \alpha_{xx}^0 e^{i(\phi(\alpha_{so}) + \phi(\alpha_{xx}))}) \\
&= \text{Re}(\alpha_{so}^0 \alpha_{xx}^0 e^{i\phi}) \\
&= \text{Re}(\alpha_{so}^0 \alpha_{xx}^0 \cos\phi - i\alpha_{so}^0 \alpha_{xx}^0 \sin\phi) \\
&= \alpha_{so}^0 \alpha_{xx}^0 \cos\phi
\end{aligned}
$$

(6)

The equation shows how the Kerr rotation ϕ_k^p is related to the two phases of the intrinsic properties α_{so} and α_{xx} owing to the excitation along x axis in the s-configurations. Clearly, the exponential notation expressions ($\alpha_{so}^0 e^{i\phi(\alpha_{so})}$ and $\alpha_{xx}^0 e^{i\phi(\alpha_{xx})}$) can definitely describe the combined phase ϕ between the two polarizations (α_{so} and α_{xx}). Clearly, by selecting proper diameters and distances between two nanopores, the combined phase can be changed enough to produce a reversal sign.

However, for the L-MOKE in s-configuration (Fig. 5b), the off-diagonal term ε_3 is activated by the magnetization along the x axis, and the new permittivity tensor can be described by the equation [7] in which all the other terms are equal to zero.

$$\varepsilon_L = \begin{pmatrix} \varepsilon_{xx} & 0 & 0 \\ 0 & \varepsilon_{yy} & i\varepsilon_3 \\ 0 & -i\varepsilon_3 & \varepsilon_{zz} \end{pmatrix}$$

(7)

Through the SO coupling, the light induced dipole P_y generates P_z.

$$P_z = \alpha_{yy}E_{so} = \alpha_{zy}E_{yy} = \frac{-i\varepsilon_3\alpha_{zz}\alpha_{yy}}{(\varepsilon - \varepsilon_m)^2}E_{yy} = \alpha_{so}\alpha_{zz}\alpha_{yy}E_{yy}$$

(8)

And the Kerr rotation ϕ_k^L in the L-MOKE configuration can be expressed as:

$$
\begin{aligned}
\phi_k^L &= \mathrm{Re}\left(\frac{p_z}{p_y}\right) = \mathrm{Re}\left(\frac{\alpha_{so}\alpha_{zz}\alpha_{yy}E_{yy}}{\alpha_{yy}E_{yy}}\right) \\
&= \mathrm{Re}(\alpha_{so}\alpha_{zz}) \\
&= \mathrm{Re}(\alpha_{so}^0 e^{i\phi(\alpha_{so})}\alpha_{zz}^0 e^{i\phi(\alpha_{zz})}) \\
&= \mathrm{Re}(\alpha_{so}^0 \alpha_{zz}^0 e^{i(\phi(\alpha_{so})+\phi(\alpha_{zz}))}) \\
&= \mathrm{Re}(\alpha_{so}^0 \alpha_{zz}^0 e^{i\phi}) \\
&= \mathrm{Re}(\alpha_{so}^0 \alpha_{zz}^0 \cos\phi - i\alpha_{so}^0 \alpha_{zz}^0 \sin\phi) \\
&= \alpha_{so}^0 \alpha_{zz}^0 \cos\phi
\end{aligned}
$$

(9)

Different from the P-MOKE configuration, ϕ_k^L is related to the two phases of the intrinsic properties α_{so} and α_{zz} due to the excitation along z axis in the s-configurations.

Conclusion

In this work, we have presented an exhaustive analysis about correlation of the hybrid multi-layered nanoporous system and the inversion sign of the Kerr hysteresis. The analysis confirms that the phases of the TM and TE electron oscillation modes account for the sign inversion of the MOKE rotation. The electron oscillation modes can be tuned at will by the surface plasmon resonance which is controlled by choosing an AAO porous film with proper pore diameter and inter-pore spacing.

The study broadens the understanding of MOKE in the nanoporous magnetoplasmonic systems. It is an opportunity to allow a more precise design of nanostructured optical and magneto-optical devices for future biotechnological applications and magneto-optical sensors.

Methods

Fabrication of Hybrid Multi-layered Nanoporous Films with Controlled AAO Substrates. Hybrid multi-layered films Ag (5 nm)/ITO (10 nm)/CoFeB (10 nm)/ITO (10 nm)/Ag (5 nm) were fabricated on the prepared six different AAO substrates, respectively, by a multi-step magnetron sputtering deposition process at room temperature[36, 37]. Noticing that the noble metallic Ag and conductive indium tin oxides (ITO) targets were sputtered in a 15 mTorr Ar gas atmosphere using the direct current (dc) sputtering apparatus (MSP-300C, WeiNa Chuangshi Inc.) with the power of 50 W. The ferromagnetic CoFeB layer was sputtered in a 0.75 mTorr Ar gas atmosphere using the radio frequency (rf) sputtering apparatus with the power of 100 W.

Characterization of the Structure and Composition. Scanning electron microscope (SEM) coupled with energy-dispersive X-ray spectroscopy (EDS) was used to characterize the top morphologies, angle tilted magnified surface information and compositions of the multi-layered nanoporous films.

Characterization of Magneto-optical Kerr Rotation and Magnetic Domain. The magneto-optical activity and the information of the magnetic domains of the prepared samples were investigated by the NanoMOKE-3 instrument (Durham Magneto Optics Ltd), a high-performance magneto-optical magnetometer and Kerr microscope, capable of both laser magnetometry and video Kerr microscopy.

With 660 nm monochromatic s-polarization light (incident angle 2°) and proper choice of a continuously changed external applied magnetic field **H** whose direction is perpendicular to the sample's surface, the polar magneto-optical Kerr effect (P-MOKE) with the magnetic field ranged from −1250 Oe to +1250 Oe with a ramp of 2.061 Oe/step was characterized. This experiment configuration was sketched in Fig. 5a.

As shown in Fig. 5b, when the direction of the magnetic field was parallel to the surface and the s-polarization light's incident angle was changed to 45°, the longitudinal magneto-optical Kerr effect (L-MOKE) information can be collected. In this experiment, similarly to the P-MOKE configuration, the excitation light wavelength was also 660 nm.

Characterization of optical response. In order to construct a reasonable model to interpret the special MO phenomena in hybridization of nanostructures and find the optical resonance position defined by the amplitude and the phase of the dipolar surface plasmon resonance (SPR) directly[109, 110], far-field absorbance was evaluated and analyzed by the conventional UV-Vis-NIR spectrophotometer (UV 3600, 190 nm-3500 nm) from 300 nm to 1000 nm at room temperature.

References

1. Barnes, W. L., Dereux, A. & Ebbesen, T. W. Surface plasmon subwavelength optics. *Nature* **424**, 824–830, doi:10.1038/nature01937 (2003).
2. Di Pietro, P. *et al.* Observation of Dirac plasmons in a topological insulator. *Nat Nano* **8**, 556–560, doi:10.1038/nnano.2013.134 (2013).
3. Won, R. View from… SMO-NP 2009: The promise of plasmonics. *Nat Photon* **3**, 500–501 (2009).
4. Cui, Y., Phang, I. Y., Hegde, R. S., Lee, Y. H. & Ling, X. Y. Plasmonic Silver Nanowire Structures for Two-Dimensional Multiple-Digit Molecular Data Storage Application. *Acs Photonics* **1**, 631–637, doi:10.1021/ph5001154 (2014).
5. O'Connor, D., McCurry, M., Lafferty, B. & Zayats, A. V. Plasmonic waveguide as an efficient transducer for high-density data storage. *Applied Physics Letters* **95**, doi:10.1063/1.3257701 (2009).
6. Lee, I.-M., Kim, S., Oh, D. & Lee, B. *In Information Optics and Optical Data Storage* Vol. 7851 *Proceedings of SPIE-The International Society for Optical Engineering* (eds F. Song *et al.*) (2010).
7. O'Connor, D. & Zayats, A. V. DATA STORAGE The third plasmonic revolution. *Nature Nanotechnology* **5**, 482–483 (2010).
8. Park, S. & Hahn, J. W. Plasmonic data storage medium with metallic nano-aperture array embedded in dielectric material. *Optics Express* **17**, 20203–20210, doi:10.1364/oe.17.020203 (2009).
9. Rodriguez-Fortuno, F. J. *et al.* Highly-sensitive chemical detection in the infrared regime using plasmonic gold nanocrosses. *Applied Physics Letters* **98**, doi:10.1063/1.3558916 (2011).
10. Matsuura, R., Tawa, K., Kitayama, Y. & Takeuchi, T. A plasmonic chip-based bio/chemical hybrid sensing system for the highly sensitive detection of C-reactive protein. *Chemical Communications* **52**, 3883–3886, doi:10.1039/c5cc07868g (2016).
11. Kong, X. *et al.* In *Frontiers in Biological Detection: From Nanosensors to Systems Viii* Vol. 9725 *Proceedings of SPIE* (eds B. L. Miller *et al.*) (2016).
12. Liang, X. *et al.* Tuning plasmonic and chemical enhancement for SERS detection on graphene-based Au hybrids. *Nanoscale* **7**, 20188–20196, doi:10.1039/c5nr06010a (2015).
13. Barbillon, G., Bijeon, J. L., Lerondel, G., Plain, J. & Royer, P. Detection of chemical molecules with integrated plasmonic glass nanotips. *Surface Science* **602**, L119–L122, doi:10.1016/j.susc.2008.06.032 (2008).
14. Pellegrotti, J. V. *et al.* Plasmonic Photothermal Fluorescence Modulation for Homogeneous Biosensing. *ACS Sens.* **1**, 1351–1357, doi:10.1021/acssensors.6b00512 (2016).
15. Tort, N., Salvador, J. P. & Marco, M. P. Multimodal plasmonic biosensing nanostructures prepared by DNA-directed immobilization of multifunctional DNA-gold nanoparticles. *Biosens. Bioelectron.* **90**, 13–22, doi:10.1016/j.bios.2016.11.022 (2017).
16. Nishiguchi, K., Sueyoshi, K., Hisamoto, H. & Endo, T. Fabrication of gold-deposited plasmonic crystal based on nanoimprint lithography for label-free biosensing application. *Japanese Journal of Applied Physics* **55**, doi:10.7567/jjap.55.08re02 (2016).
17. Hinman, S. S. & Cheng, Q. Bioinspired assemblies and plasmonic interfaces for electrochemical biosensing. *Journal of Electroanalytical Chemistry* **781**, 136–146, doi:10.1016/j.jelechem.2016.05.014 (2016).
18. Castro Arias, J., Cattoni, A., Decanini, D., Collin, S. & Haghiri-Gosnet, A. M. *Biosensing on a Chip: Study of Plasmonic Nanostructures Integrated in Microfluidic Devices.* (2017).
19. Aristov, A. I. *et al.* 3D plasmonic crystal metamaterials for ultra-sensitive biosensing. *Scientific Reports* **6**, doi:10.1038/srep25380 (2016).
20. Vinogradov, A. P. *et al.* In *Magnetophotonics: From Theory to Applications* (eds Mitsuteru Inoue, Miguel Levy, & Alexander V. Baryshev) 1–17 (Springer Berlin Heidelberg, 2013).
21. Uchida, K. *et al.* Generation of spin currents by surface plasmon resonance. *Nat Commun* **6**, 5910, doi:10.1038/ncomms6910 (2015).
22. Belotelov, V. I., Kalish, A. N. & Zvezdin, A. K. In *Magnetophotonics: From Theory to Applications* (eds Mitsuteru Inoue, Miguel Levy, & Alexander V. Baryshev) 51-106 (Springer Berlin Heidelberg, 2013).
23. Song, Y. *et al.* Identification of single nanoparticles. *Nanoscale* **3**, 31–44, doi:10.1039/C0NR00412J (2011).
24. Song, Y. Controlled Fabrication of Noble Metal Nanomaterials via Nanosphere Lithography and Their Optical Properties. doi:10.5772/25037 (2011).
25. Maksymov, I. S. Magneto-Plasmonics and Resonant Interaction of Light with Dynamic Magnetisation in Metallic and All-Magneto-Dielectric Nanostructures. *Nanomaterials* **5**, 577–613, doi:10.3390/nano5020577 (2015).
26. Temnov, V. V. Ultrafast acousto-magneto-plasmonics. *Nature Photonics* **6**, 728–736, doi:10.1038/nphoton.2012.220 (2012).
27. Li, J., Zhang, W., Song, Y., Yin, W. & Zhang, T. Template Transfer Nanoimprint for Uniform Nanopores and Nanopoles. *Journal of Nanomaterials*, doi:10.1155/2016/9354364 (2016).
28. Jiang, S. *et al.* Study on Light Extraction from GaN-based Green Light-Emitting Diodes Using Anodic Aluminum Oxide Pattern and Nanoimprint Lithography. *Sci Rep* **6**, 21573, doi:10.1038/srep21573 (2016).
29. Hua Yu, F. *et al.* Magnetoplasmonics in split ring-ring structures fabricated with hole-mask colloidal lithography. *2016 Progress in Electromagnetic Research Symposium* (*PIERS*), 751–751, doi:10.1109/piers.2016.7734446 (2016).
30. Feng, H. Y. *et al.* Magnetoplasmonic Nanorings as Novel Architectures with Tunable Magneto-optical Activity in Wide Wavelength Ranges. *Advanced Optical Materials* **2**, 612–617, doi:10.1002/adom.201400125 (2014).
31. Feng, H. Y., Luo, F., Meneses-Rodriguez, D., Armelles, G. & Cebollada, A. From disk to ring: Aspect ratio control of the magnetoplasmonic response in Au/Co/Au nanostructures fabricated by hole-mask colloidal lithography. *Applied Physics Letters* **106**, doi:10.1063/1.4913621 (2015).
32. Armelles, G. *et al.* Magnetoplasmonic nanostructures: systems supporting both plasmonic and magnetic properties. *Journal of Optics a-Pure and Applied Optics* **11**, doi:10.1088/1464-4258/11/11/114023 (2009).
33. Banthi, J. C. *et al.* In *Nanophotonics Iv* Vol. 8424 *Proceedings of SPIE* (eds D. L. Andrews, J. M. Nunzi, & A. Ostendorf) (2012).
34. Feng, H. Y. *et al.* Active magnetoplasmonic split-ring/ring nanoantennas. *Nanoscale* **9**, 37–44, doi:10.1039/c6nr07864h (2017).
35. Gonzalez-Diaz, J. B. *et al.* Plasmonic Au/Co/Au nanosandwiches with enhanced magneto-optical activity. *Small* **4**, 202–205, doi:10.1002/smll.200700594 (2008).
36. Song, Y., Wang, Y., Li, B. B., Fernandes, C. & Ruda, H. E. Interface interaction induced ultra-dense nanoparticles assemblies. *Nanoscale* **5**, 6779, doi:10.1039/c3nr01366a (2013).
37. Song, Y. *et al.* Magneto-Plasmons in Periodic Nanoporous Structures. *Scientific Reports* **4**, doi:10.1038/srep04991 (2014).
38. Song, Y., Zhang, T., Yang, W., Albin, S. & Henry, L. L. Fine crystal structure transition of cobalt nanoparticles formed in a microfluidic reactor. *Crystal Growth & Design* **8**, 3766–3772, doi:10.1021/cg8003992 (2008).
39. Wang, J. *et al.* Microfluidic synthesis of ultra-small magnetic nanohybrids for enhanced magnetic resonance imaging. *J. Mater. Chem. C* **3**, 12418–12429, doi:10.1039/c5tc02279g (2015).
40. Song, Y. & Henry, L. L. Nearly Monodispersion CoSm Alloy Nanoparticles Formed by an *In-situ* Rapid Cooling and Passivating Microfluidic Process. *Nanoscale Res. Lett.* **4**, 1130, doi:10.1007/s11671-009-9369-8 (2009).
41. Uchida, H., Masuda, Y., Fujikawa, R., Baryshev, A. V. & Inoue, M. Large enhancement of Faraday rotation by localized surface plasmon resonance in Au nanoparticles embedded in Bi:YIG film. *Journal of Magnetism and Magnetic Materials* **321**, 843–845, doi:10.1016/j.jmmm.2008.11.064 (2009).
42. Maksymov, I. S. Magneto-plasmonic nanoantennas: basics and applications (Review) arXiv. *arXiv*, 15 pp.-15 pp. (2016).
43. Liang, H. *et al.* Giant enhancement of Kerr rotation in two-dimensional Bismuth iron garnet/Ag photonic crystals. *Chinese Physics B* **24**, doi:10.1088/1674-1056/24/6/067807 (2015).

44. Yamane, H., Takeda, K. & Kobayashi, M. Fabrication and magneto-optical properties of perpendicular magnetic CoPt nanostructures formed by surface agglomeration of Ag. *Japanese Journal of Applied Physics* **54**, doi:10.7567/jjap.54.06fj09 (2015).
45. Yamane, H., Takeda, K. & Kobayashi, M. Magneto-Optical Enhancement and Chemical Sensing Applications of Perpendicular Magnetic CoPt/Ag Stacked Structures with a ZnO Intermediate Layer. *Materials Transactions* **57**, 892–897, doi:10.2320/matertrans.M2015395 (2016).
46. Hamidi, S. M. & Ghaebi, O. Enhanced magneto-plasmonic effect in Au/Co/Au multilayers caused by exciton-plasmon strong coupling. *Journal of Magnetism and Magnetic Materials* **414**, 122–125, doi:10.1016/j.jmmm.2016.04.060 (2016).
47. Kravets, A. F., Borodnova, T. I. & Kravets, V. G. Strong plasmon enhancement of magneto-optical Kerr rotation in Co-AlO nanogranular films coated with gold nanoparticles. *Journal of the Optical Society of America B-Optical Physics* **33**, 302–307, doi:10.1364/josab.33.000302 (2016).
48. Li, J., Tang, T., Zhang, Y. & Luo, L. Enhancement of the transverse magneto-optical Kerr effect via resonant tunneling in Au/Ce:YIG/Au trilayers and its application. *Laser Physics* **27**, doi:10.1088/1555-6611/aa4ff4 (2017).
49. Bossini, D., Belotelov, V. I., Zvezdin, A. K., Kalish, A. N. & Kimel, A. V. Magnetoplasmonics and Femtosecond Optomagnetism at the Nanoscale. *Acs Photonics* **3**, 1385–1400, doi:10.1021/acsphotonics.6b00107 (2016).
50. Bonanni, V. *et al*. Designer Magnetoplasmonics with Nickel Nanoferromagnets. *Nano Letters* **11**, 5333–5338, doi:10.1021/nl2028443 (2011).
51. Lodewijks, K. *et al*. Magnetoplasmonic Design Rules for Active Magneto-Optics. *Nano Letters* **14**, 7207–7214, doi:10.1021/nl504166n (2014).
52. Northup, T. E. & Blatt, R. Quantum information transfer using photons. *Nature Photonics* **8**, 356–363, doi:10.1038/nphoton.2014.53 (2014).
53. Peyronel, T. *et al*. Quantum nonlinear optics with single photons enabled by strongly interacting atoms. *Nature* **488**, 57–60, doi:10.1038/nature11361 (2012).
54. Chen, J. Y. *et al*. Time-Resolved Magneto-Optical Kerr Effect of Magnetic Thin Films for Ultrafast Thermal Characterization. *The journal of physical chemistry letters* **7**, 2328–2332, doi:10.1021/acs.jpclett.6b00945 (2016).
55. Song, Y. *et al*. Microfluidic synthesis of cobalt nanoparticles. *Chem. Mater.* **18**, 2817–2827 (2006).
56. Kreibig, U. & Vollmer, M. *Optical Properties of Metal Clusters*. (Springer, 1995).
57. Belotelov, V. I. *et al*. Enhanced magneto-optical effects in magnetoplasmonic crystals. *Nature Nanotechnology* **6**, 370–376, doi:10.1038/nnano.2011.54 (2011).
58. Walter, E. *Metal clusters* (*Chichester, New York: Wiley*) (1999).
59. Kazuma, M., Takehito, K. & Tsuguo, S. *Anal. Chem* **70**, 5037–5041 (1998).
60. Nie, S. & Emory, S. R. Probing Single Molecules and Single Nanoparticles by Surface-Enhanced Raman Scattering. *Science* **275**, 1102–1106 (1997).
61. Kim, H. B. *et al*. *Anal. Chem.* **68**, 409 (1996).
62. Xu, X.-H. N. & Patel, R. N. *Imaging and Assemble of Nanoparticles in Biological Systems. In Handbook of Nanostructured Biiomaterials and their Applications in Nanobiotechnology (Ed. Nalwa H S), p 1–22.* Vol. 1 (2005).
63. Armelles, G., Cebollada, A., García-Martín, A. & González, M. U. Magnetoplasmonics: Combining Magnetic and Plasmonic Functionalities. *Advanced Optical Materials* **1**, 10–35, doi:10.1002/adom.201200011 (2013).
64. Raschke, G. *et al*. *Nano Letters* **3**, 935–938 (2003).
65. González-Díaz, J. B. *et al*. Enhanced Magneto-Optics and Size Effects in Ferromagnetic Nanowire Arrays. *Advanced Materials* **19**, 2643–2647, doi:10.1002/adma.200602938 (2007).
66. Song, Y. *et al*. Investigations into sulfobetaine-stabilized Cu nanoparticle formation: toward development of a microfluidic synthesis. *J. Phys. Chem. B* **109**, 9330–9338 (2005).
67. Wurtz, G. A. *et al*. Controlling optical transmission through magneto-plasmonic crystals with an external magnetic field. *New Journal of Physics* **10**, 105012, doi:10.1088/1367-2630/10/10/105012 (2008).
68. González-Díaz, J. B. *et al*. Plasmonic Au/Co/Au Nanosandwiches with Enhanced Magneto-optical Activity. *Small* **4**, 202–205, doi:10.1002/smll.200700594 (2008).
69. Du, G. X., Mori, T., Saito, S. & Takahashi, M. Shape-enhanced magneto-optical activity: Degree of freedom for active plasmonics. *Physical Review B* **82**, doi:10.1103/PhysRevB.82.161403 (2010).
70. Van Duyne, R. P., Haes, A. J. & McFarland, A. D. *Proceedings of SPIE, 5223, Physical chemistry of Interfaces and Nanomaterials II* (*SPIE, Belingham, WA*). (SPIE, 2003).
71. Tomita, S. *et al*. Magneto-Optical Kerr Effects of Yttrium-Iron Garnet Thin Films Incorporating Gold Nanoparticles. *Physical Review Letters* **96**, doi:10.1103/PhysRevLett.96.167402 (2006).
72. Wang, L. *et al*. Plasmonics and Enhanced Magneto-Optics in Core-Shell Co-Ag Nanoparticles. *Nano Letters* **11**, 1237–1240, doi:10.1021/nl1042243 (2011).
73. Liu, Z. *et al*. Magneto-optical Kerr effect in perpendicularly magnetized Co/Pt films on two-dimensional colloidal crystals. *Applied Physics Letters* **95**, 032502, doi:10.1063/1.3182689 (2009).
74. Thompson, G. E., Furneaux, R. C., Wood, G. C., Richardson, J. A. & Goode, J. S. Nucleation and growth of porous anodic films on aluminium. *Nature* **272**, 433–435, doi:10.1038/272433a0 (1978).
75. Jessensky, O., Müller, F. & Gösele, U. Self-organized formation of hexagonal pore arrays in anodic alumina. *Applied Physics Letters* **72**, 1173–1175, doi:10.1063/1.121004 (1998).
76. Masuda, H., Hasegwa, F. & Ono, S. Self-ordering of cell arrangement of anodic porous alumina formed in sulfuric acid solution. *Journal of the Electrochemical Society* **144**, L127–130, doi:10.1149/1.1837634 (1997).
77. Huber, C. A. *et al*. Nanowire array composites. *Science (New York, N. Y.)* **263**, 800–802, doi:10.1126/science.263.5148.800 (1994).
78. Song, Y., Wang, Y., Li, B. B., Fernandes, C. & Ruda, H. E. Interface interaction induced ultra-dense nanoparticles assemblies. *Nanoscale* **5**, 6779–6789, doi:10.1039/c3nr01366a (2013).
79. Awad, A. M., Shehata, O. S. & Heakal, F. E. T. Effect of various de-anodizing techniques on the surface stability of non-colored and colored nanoporous AAO films in acidic solution. *Applied Surface Science* **359**, 939–947, doi:10.1016/j.apsusc.2015.10.221 (2015).
80. Kikuchi, T., Nishinaga, O., Natsui, S. & Suzuki, R. O. Self-Ordering Behavior of Anodic Porous Alumina via Selenic Acid Anodizing. *Electrochimica Acta* **137**, 728–735, doi:10.1016/j.electacta.2014.06.078 (2014).
81. Cepak, V. M. *et al*. Chemical Strategies for Template Syntheses of Composite Micro- and Nanostructures. *Chemistry of Materials* **9**, 1065–1067, doi:10.1021/cm970014c (1997).
82. Lee, W., Ji, R., Goesele, U. & Nielsch, K. Fast fabrication of long-range ordered porous alumina membranes by hard anodization. *Nature Materials* **5**, 741–747, doi:10.1038/nmat1717 (2006).
83. Karmhag, R., Tesfamichael, T., Wackelgard, E., Niklasson, A. & Nygren, M. Oxidation kinetics of nickel particles: Comparison between free particles and particles in an oxide matrix. *Solar Energy* **68**, 329–333, doi:10.1016/s0038-092x(00)00025-6 (2000).
84. Che, G., Lakshmi, B. B., Fisher, E. R. & Martin, C. R. Carbon nanotubule membranes for electrochemical energy storage and production. *Nature* **393**, 346–349 (1998).
85. Che, G. L., Lakshmi, B. B., Martin, C. R. & Fisher, E. R. Metal-nanocluster-filled carbon nanotubes: Catalytic properties and possible applications in electrochemical energy storage and production. *Langmuir* **15**, 750–758, doi:10.1021/la980663i (1999).
86. Che, G., Lakshmi, B. B., Martin, C. R., Fisher, E. R. & Ruoff, R. S. Chemical Vapor Deposition Based Synthesis of Carbon Nanotubes and Nanofibers Using a Template Method. *Chemistry of Materials* **10**, 260–267, doi:10.1021/cm970412f (1998).

87. Byung, J. L. Method for manufacturing metal oxide nanostructure of porous network structure, involves injecting photo catalyst substance precursor into anode oxidation aluminum (AAO) template. KR2015021095-A (2015).
88. Wang, Q., Shimizu, T. & Shingubara, S. *Control of crystalline orientation and diameter of Si nanowires based on VLS method and electrodeposition of catalyst using AAO template.* (2011).
89. Ibanes, J. J. *et al. In Physics of Semiconductors: 30th International Conference on the Physics of Semiconductors* Vol. 1399 *AIP Conference Proceedings* (eds J. Ihm & H. Cheong) (2011).
90. Nielsch, K. *et al.* Hexagonally ordered 100 nm period nickel nanowire arrays. *Applied Physics Letters* **79**, 1360–1362, doi:10.1063/1.1399006 (2001).
91. Furneaux, R. C., Rigby, W. R. & Davidson, A. P. The formation of controlled-porosity membranes from anodically oxidized aluminium. *Nature* **337**, 147–149, doi:10.1038/337147a0 (1989).
92. Chaturvedi, P., Rodriguez, S. D., Vlassiouk, I., Hansen, I. A. & Smirnov, S. N. Simple and Versatile Detection of Viruses Using Anodized Alumina Membranes. *ACS Sens.* **1**, 488–492, doi:10.1021/acssensors.6b00003 (2016).
93. Alzghoul, S., Hailat, M., Zivanovic, S., Que, L. & Shah, G. V. Measurement of serum prostate cancer markers using a nanopore thin film based optofluidic chip. *Biosens. Bioelectron* **77**, 491–498, doi:10.1016/j.bios.2015.10.006 (2016).
94. Silina, Y. E., Kychmenko, T. A. & Koch, M. Nanoporous anodic aluminum oxide films for UV/vis detection of noble and non-noble metals. *Anal. Methods* **8**, 45–51, doi:10.1039/c5ay02498f (2016).
95. Lee, S. B. *et al.* Antibody-based bio-nanotube membranes for enantiomeric drug separations. *Science* **296**, 2198–2200, doi:10.1126/science.1071396 (2002).
96. Taberna, L., Mitra, S., Poizot, P., Simon, P. & Tarascon, J. M. High rate capabilities Fe3O4-based Cu nano-architectured electrodes for lithium-ion battery applications. *Nature Materials* **5**, 567–573, doi:10.1038/nmat1672 (2006).
97. Lombardi, I., Magagnin, L., Cavallotti, P. L., Carraro, C. & Maboudian, R. Electrochemical fabrication of supported Ni nanostructures through transferred porous anodic alumina mask. *Electrochemical and Solid State Letters* **9**, D13–D16, doi:10.1149/1.2181287 (2006).
98. Li, F., Zhang, L. & Metzger, R. M. On the growth of highly ordered pores in anodized aluminum oxide. *Chem. Mater.* **10**, 2470–2480 (1998).
99. Norek, M. *et al.* Multi-band emission in a wide wavelength range from tin oxide/Au nanocomposites grown on porous anodic alumina substrate (AAO). *Applied Surface Science* **287**, 143–149, doi:10.1016/j.apsusc.2013.09.101 (2013).
100. Högemann, D., Josephson, L., Weissleder, R. & Basilion, J. P. *Bioconjug. Chem.* **11**, 941–946 (2000).
101. Santos, A. *et al.* Tunable Fabry-Perot interferometer based on nanoporous anodic alumina for optical biosensing purposes. *Nanoscale Res. Lett.* **7**, 4, doi:10.1186/1556-276x-7-370 (2012).
102. Gardelis, S., Nassiopoulou, A. G., Gianneta, V. & Theodoropoulou, M. Photoluminescence-induced oscillations in porous anodic aluminum oxide films grown on Si: Effect of the interface and porosity. *Journal of Applied Physics* **107**, doi:10.1063/1.3432694 (2010).
103. Berciaud, S. *et al.* Ultrasensitive and Single-Molecule Detection Technologies. *Proceedings of SPIE-The international Society for Optical Engineering* **6092** 60920A/60921-60920A/60928 (2006).
104. Muskens O. L., D. F. N., Vallee F., Huntzinger J. R., Billaud P. & Broyer M. *App. Phys. Lett.* **88**, 063109 (2006).
105. Chan, S., Okuyama, K., M., D. L. & Juan, F. *Aerosol Science and Technology* **37**, 791–803 (2003).
106. Maccaferri, N. *et al.* Tuning the Magneto-Optical Response of Nanosize Ferromagnetic Ni Disks Using the Phase of Localized Plasmons. *Physical Review Letters* **111**, 5, doi:10.1103/PhysRevLett.111.167401 (2013).
107. Chin, J. Y. *et al.* Nonreciprocal plasmonics enables giant enhancement of thin-film Faraday rotation. *Nature Communications* **4**, 1599, doi:10.1038/ncomms2609 (2013).
108. Maccaferri, N. *et al.* Ultrasensitive and label-free molecular-level detection enabled by light phase control in magnetoplasmonic nanoantennas. *Nature Communications* **6**, 6150, doi:10.1038/ncomms7150 (2015).
109. Graham, D. L., Ferreira, H. A. & Freitas, P. P. *Trends in Biotechnology* **22**, 455–462 (2004).
110. Maccaferri, N. *et al.* Effects of a non-absorbing substrate on the magneto-optical Kerr response of plasmonic ferromagnetic nanodisks. *physica status solidi (a)* **211**, 1067–1075, doi:10.1002/pssa.201300701 (2014).

Acknowledgements

Author Contributions

W.W.Zhang, J.J.Li and X.K.Ding planned the experiments. Y.J.Song, W.W.Zhang and J.J.Li performed the experiment. Y.J.Song, W.W.Zhang, P.Pernod and N.Tiercelin analyzed the data. Y.J. Song and W.W. Zhang wrote the main manuscript text. All authors have approved the final version of the manuscript.

Additional Information

Supplementary information accompanies this paper at doi:10.1038/s41598-017-03241-7

Competing Interests: The authors declare that they have no competing interests.

Publisher's note: Springer Nature remains neutral with regard to jurisdictional claims in published maps and institutional affiliations.